RESEARCH ARTICLE

WILEY

Effects of atmospheric stability on the structural response of a 12 MW semisubmersible floating wind turbine

Irene Rivera-Arreba[1] | Adam S. Wise[2] | Mahé Hermile[1] | Fotini K. Chow[2] |
Erin E. Bachynski-Polić[1]

[1]Department of Marine Technology,
Norwegian University of Science and
Technology, Trondheim, Norway

[2]Civil and Environmental Engineering,
University of California, Berkeley, Berkeley,
California, USA

Correspondence
Irene Rivera-Arreba, Department of Marine
Technology, Norwegian University of Science
and Technology, Trondheim, Norway.
Email: irene.rivera.arreba@ntnu.no

Abstract

Global dynamic response models used for the design of wind turbines are largely based on neutral stability, which is not representative of real atmospheric conditions. Offshore wind farms, for example, have been seen to experience predominantly unstable conditions, especially at lower wind speeds. In the current work, we use four wind generation models under stable, neutral and unstable atmospheric stability conditions to study the low-frequency content of the global responses of a semisubmersible floating wind turbine (FWT). To represent the wind fields, we use the Kaimal Spectrum and Exponential Coherence Model (Kaimal), the Mann Spectral Tensor Model (Mann), a point measurement based model (TIMESR) and large-eddy simulation (LES). At the low-frequency range, both atmospheric stability and the turbulence wind model significantly affect the response of the FWT. In all the cases studied throughout this paper, the structural response under unstable conditions is higher than under stable or neutral conditions. The TIMESR and the Kaimal models fitted to the FINO-1 offshore meteorological mast measurements show more similar responses than the Mann model; surge and pitch are higher for the TIMESR and Kaimal models, and yaw is lower. When fitted to LES, TIMESR and Kaimal predict surge and pitch responses closer to LES, but they underestimate the responses related to yaw, opposite to what the Mann model does. The responses are directly related to turbulence intensity and coherence, which are affected by atmospheric stability. Therefore, based on the analyses carried out through this study, the structural analysis of FWT should account for the effect of atmospheric stability.

KEYWORDS
atmospheric stability, FINO-1, floating wind turbines, Kaimal, LES, Mann, TIMESR

1 | INTRODUCTION

To achieve a fully economically viable way to harness wind energy in intermediate and deep water depths, further cost reductions and design improvements are needed in the floating wind energy industry. The effect of atmospheric stability on the loading of onshore and bottom-fixed wind turbines has been well studied.[1–3] However, its effect on the response and motions of floating wind turbines (FWT) has not been studied to

such a large extent, especially for semisubmersible substructures. Atmospheric stability has a significant effect on parameters such as turbulence intensity, shear and coherence, which drive FWT response. Notably, unstable atmospheric conditions are characterised by a lack of shear, high turbulence intensity and large coherent structures, while stable conditions are strongly sheared with much lower turbulence intensity and very small coherent structures. These characteristics strongly affect FWT motions in various ways. The aim is to analyse the effect of atmospheric stability on the response of a semisubmersible FWT.

Currently, there are two wind turbulence models recommended by the International Electrotechnical Commission (IEC),[4] namely, the Kaimal Spectrum and Exponential Coherence Model[5] (here called *Kaimal*) and the Mann Spectral Tensor Model[6,7] (here called *Mann*). Both models have an identical frequency content, but the spatial coherence differs. The Mann model was validated with measurements taken on the Great Belt Bridge in Denmark,[6] and the Kaimal model is based on measurements onshore in Kansas.[8] The validation of both models was done under stable atmospheric conditions. Doubrawa et al[9] and Eliassen and Obhrai[10] compared the wind fields generated by these two models to large-eddy simulation (LES) and to point measurements, respectively. For low wind speeds, Doubrawa et al. found that the Mann model more closely resembled both their LES data and the point measurements. For higher wind speeds, the Kaimal model showed closer results to the LES, while the Mann model was closer to the measurements. Due to the low natural frequencies of FWT, the effects of the wind models on the low-frequency range are very relevant.[11–13] Most of the previous studies that compared the response of FWT using the two models recommended by the IEC guidelines assumed neutral stability conditions and therefore used constant standard parameters. However, earlier research has shown that offshore wind farms experience predominantly unstable conditions, especially at lower wind speeds.[14,15] The main parameters affected by atmospheric stability are the wind speed at hub height (HH), turbulence intensity, wind shear, coherence and wake recovery. These parameters are a function of atmospheric stability,[1,16] and therefore, not only the choice of wind turbulence model is of relevance but also the effect that atmospheric stability has on the model itself. The procedure to account for stability in the models recommended by the IEC guidelines may be based on measurements or on higher-fidelity models such as LES.

Most of the work to date which studies atmospheric stability combined with offshore wind turbines focuses either on the effect of stability on fixed structures, e.g., Nybø et al.,[3] or on the effect of the turbulence model and coherence on FWT under neutral conditions, e.g., Bachynski & Eliassen.[12] Doubrawa et al.,[9] Nybø et al.[17] and Myrtvedt et al.[18] studied the effect of atmospheric stability on a spar-type FWT. The effect of atmospheric stability on the global motions and on the structural response of a semisubmersible FWT has not previously been studied using the Kaimal and Mann models fitted to LES data and point measurements. In the current work, we study the effect of atmospheric stability on the response of the INO WINDMOOR 12 MW semisubmersible floating wind turbine.[19] To model the semisubmersible FWT, we use the aero-hydro-servo-elastic tool OpenFAST 2.5.0,[20] developed at the National Renewable Energy Laboratory (NREL); more details on the modelling are included in Section 3. First, the Kaimal and Mann models are applied, based on input parameters which depend on atmospheric stability. When tuning the LES data to the FINO-1 point measurements there are slight differences in ambient wind statistics; to better quantify and compare stability effects, we fit the synthetic models to the LES data and the FINO-1 measurements separately. Therefore, the parameters for the Kaimal and Mann models are obtained from two sets of data: The first set of data consists of the point measurements from the FINO-1 offshore meteorological mast, and the second set is based on high-fidelity LES data. Second, the TIMESR option given within TurbSim,[21] the turbulence simulator developed at NREL, is used based on the point measurements from the FINO-1 platform, and, separately, on the set of high-fidelity LES data. Lastly, the wind fields generated by the Weather Research and Forecasting (WRF) model's[22] LES capability under stable, neutral and unstable atmospheric conditions, which are previously used to fit the Kaimal and Mann models input parameters, are directly used as input to OpenFAST. We study nine cases, comprised of three stability conditions and three mean wind speeds at hub height, which cover rated scenario and below-rated and over-rated scenarios in which the turbine operates with similar thrust levels. Six 1-h realisations are performed, based on the findings of Kvittem et al,[23] where the convergence of fatigue estimates for different simulation length and number of simulations is investigated.

The current work is divided into the analysis of the FINO-1 measurements and the LES wind field generation and the subsequent comparison of the structural response of the INO WINDMOOR 12MW FWT. Section 2 gives an overview of the processing of FINO-1 data, their classification into stability conditions and how the parameters inherent to the Kaimal, Mann and TIMESR models are obtained, based on both FINO-1 measurements and the LES data. Furthermore, the LES setup is described in the same section. Section 3 describes the INO WINDMOOR 12 MW model as implemented in OpenFAST 2.5.0. Section 4 analyses the structural response for the conditions examined in this study.

2 | METHODOLOGY

2.1 | Environmental conditions

The environmental conditions (ECs) used in this work are based on the wind measurements at the offshore mast FINO-1[24] and on the hindcast data of 1-h averaged sea states placed on a 200 m depth reference site in the North Sea. Three representative cases based on the long-term joint distribution from Li et al[25] at three wind speeds (below-, close to- and above-rated) are selected. The significant wave height H_s, peak period T_p

TABLE 1 Environmental conditions used in this work for the three mean wind speed scenarios

EC	U_w [m/s]	H_s [m]	T_p [s]
EC1	7.5	2.3	8.3
EC2	12	2.9	8.4
EC3	16	3.5	8.6

and mean wind speed at hub height U_w are indicated for the three ECs in Table 1. Each environmental condition is studied for stable, neutral and unstable atmospheric stratification.

To generate the ambient wind fields, we use four turbulence models, namely, Kaimal, Mann, TIMESR and the LES. The input parameters for the Kaimal, Mann and TIMESR models are fitted separately to the FINO-1 measurements and the high-fidelity LES data. The aim was to have the mean wind speed at hub height, TI and shear of the LES data similar to the FINO-1 measurements. Due to the nature of LES, however, the parameters are close but not able to be exactly matched. Therefore, rather than directly comparing models fitted to FINO-1 to the LES and FINO-1 measurements, two sets of models are compared: (1) the Kaimal, Mann and TIMESR models fitted to the FINO-1 data and (2) the Kaimal, Mann and TIMESR models fitted to LES data.

2.2 | FINO-1 measurements

2.2.1 | Data filtering and analysis

The FINO-1 platform is located in the North Sea and is equipped with meteorological sensors for wind, temperature and humidity.[24] In this work, high-frequency (20 Hz) wind speed data measured by ultrasonic anemometers at 41, 61 and 81 m, and 10-min averaged wind speed data extracted from the high-frequency ultrasonic measurements, are used. The measurements used in the current work cover a 2-year time period, from 1 January 2016 to 31 December 2017.

To divide the measurements into stability classes, we use the 10-min averaged data from the ultrasonic anemometers, which are processed in the following steps:

- missing measurements and spikes are removed,
- data from the specific zone affected by the mast shadow, wind farm proximity and nearby land are removed, i.e., between 45° and 225°,
- the data are organised in 1-h periods and
- non-stationary periods are deleted, following the criteria from Cheynet et al.[26]

Once the 10-min averaged data are processed, the wind shear profile is computed by using the data from the cup anemometers provided at heights from 34 to 101 m high, every 10 m. These data are selected based on the classification of the measurements into atmospheric stability classes, as presented in Section 2.2.2. To get the mean wind speed at hub height, we use the power law, as explained in Section 2.4. The time series are selected based on the specific criteria of mean wind speed and atmospheric stability. When the time series are selected, the high-frequency 1-h data from the ultrasonic anemometers are extracted to compute the turbulence intensity, to obtain the Mann model parameters and to fit the coherence models for Kaimal and TIMESR.

2.2.2 | Atmospheric stability classification

The most relevant physical parameters that define the atmospheric boundary layer (BL) region, where wind turbines operate, are the fluxes of momentum, heat and moisture. These parameters directly affect atmospheric stability, since they have a direct effect on thermal stratification. One of the most commonly used methods to classify atmospheric stability is the Pasquill-Gifford-Turner (PGT) criterion, which classifies stability ranging from very stable to very unstable stratification.[27] In this work, the stability classification is done based on the Richardson number Ri,[28] which relates buoyancy-generated turbulence with turbulence produced by shear as:

$$Ri = \frac{g}{T} \frac{(\Delta\theta/\Delta z)}{(\Delta u/\Delta z)^2},$$

(1)

TABLE 2 Stability classification based on the Richardson number[29]

Stability class	VU	U	NU	N
Range	$R_i < -5.34$	$-5.34 < R_i < 2.26$	$-2.26 < R_i < 0.569$	$-0.569 < R_i < 0.083$

Abbreviations: VU, very unstable; U, unstable; NU, near unstable; N, neutral; NS, near stable; S, stable; VS, very stable.

TABLE 2 (Continued)

Stability class	NS	S	VS
Range	$0.083 < R_i < 0.196$	$0.196 < R_i < 0.49$	$0.49 < R_i$

Abbreviations: VU, very unstable; U, unstable; NU, near unstable; N, neutral; NS, near stable; S, stable; VS, very stable.
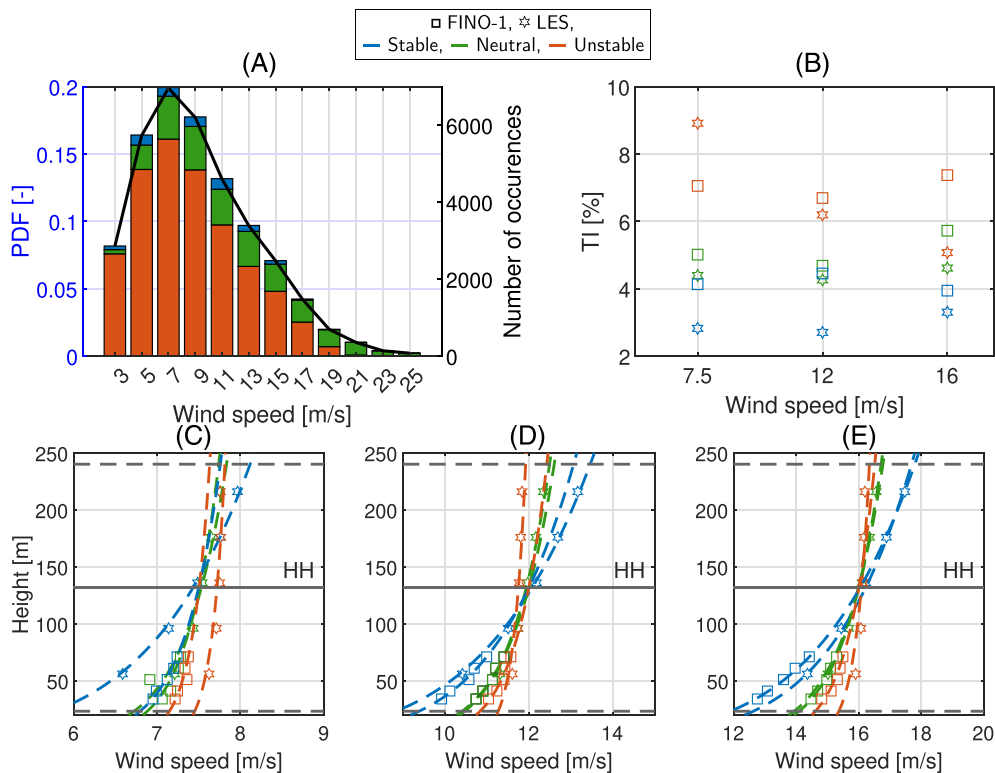

FIGURE 1 (A) Distribution of atmospheric stability as a function of wind speed at 81 m. The y axis shows the mean of the lower and upper limits of the specific bin. (B) TI for each wind speed and stability condition at 81 m for the FINO-1 and at hub height for the LES data. The squares and the stars represent FINO-1 and LES data, respectively. (C–E) Wind profile for each wind speed and atmospheric stability condition. The horizontal dashed lines indicate the upper and lower limits of the INO WINDMOOR 12MW FWT rotor, whereas the horizontal solid line represents the hub height

where θ is the potential temperature, T is the mean temperature, $\Delta u/\Delta z$ is the velocity gradient and g the gravity constant. The Richardson classification is shown in Table 2: In this work, the *very unstable*, *near unstable* and *unstable* conditions are lumped into *unstable*, while the *very stable*, *near stable* and *stable* conditions are grouped into *stable*. The temperature data used to classify the measurements are those at 72 and 42 m. The wind speed measurements are extracted at 91 and 71 m, from the cup anemometers. Figure 1A shows the resulting atmospheric stability distribution, where the predominance of unstable conditions, especially at lower wind speeds, is seen. This distribution is consistent with previous findings on FINO-1 data.[15]

2.3 | Large eddy simulation

In this work, we use LES to simulate the marine atmospheric boundary layer. LES explicitly solves the most energetic eddies while parameterising the effects of the smaller turbulent length scales on the resolved-scale flow. LES can therefore capture transient turbulent flow structures, which are important features of the atmospheric boundary layer that interact with FWTs.

We use the idealised LES capability of the WRF model.[22] This tool is a non-hydrostatic, fully compressible solver of the Euler equations including the Coriolis term. The base code is from WRF version 4.2.2, and modifications to the source code include a surface layer parameterization[30] that allows for surface cooling (used to simulate the stable boundary layer) and a method to output y-z planes at each model time-step. The LES is run using a third-order Runge-Kutta time advancement scheme, with fifth-order horizontal and third-order vertical advection schemes. We use a vertical grid resolution of 8 m from 0–250 m a.s.l., after which the grid spacing increases logarithmically to 40 m at the domain top of 2 km. We use Monin-Obukhov similarity theory[31] at the surface (using the aforementioned modification) and a Rayleigh damping layer for the top 500 m of the domain. The smaller turbulent length scales are parameterised using the turbulent kinetic energy (TKE) order 1.5 LES closure.[32]

The values for the surface roughness to represent wave heights are obtained from the work of Archer et al[33] with $9.0 \text{ m} \cdot 10^{-5}$ corresponding to unstable conditions, $6.05 \text{ m} \cdot 10^{-5}$ corresponding to neutral conditions, and $5.25 \text{ m} \cdot 10^{-5}$ corresponding to stable conditions. The surface heat flux is set to 0.05 K m/s (60 W/m²) for unstable conditions, and we use a cooling rate of −0.2 K/h for stable conditions. The latitude is set to 54.014861°, which is the same latitude as the FINO-1 platform. The initial geostrophic wind speed profiles are tuned for the target mean hub height wind speeds. For the unstable and neutral BLs, the initial potential temperature profile is neutrally stratified up to 700 m, after which an inversion of 4 K/km for unstable conditions and 10 K/km for neutral conditions is imposed. For the stable BLs, the potential temperature profile is also neutrally stratified but only until 100 m, followed by an inversion of 10 K/km. For the rated and above-rated wind speed cases, the height of the inversion increases to above the rotor plane with simulation time as a low-level jet develops; however, for the below-rated wind speed case, the initial inversion is specified at 250 m to ensure that the rotor plane is within the region of positive shear below the low-level jet. These initial condition profiles are chosen to follow the setups of Peña et al.[34]

For the unstable and neutral BLs, we use a one-way nested domain setup. The parent domain has a grid resolution of 24 m in the horizontal and a domain size of 60 km × 14.4 km. Periodic boundary conditions are applied in the lateral direction, and the time-step is 0.5 s. The child domain has a grid resolution of 8 m in the horizontal, a domain size of 4 km × 2 km and a time-step of 0.1 s with inflow conditions coming from the parent domain. This setup allows for the low-frequency, large-scale coherent structures (which can be on the order of kilometres for unstable and neutral BLs) to develop on the parent domain, which then cascade into smaller-scale, higher-frequency turbulence in the child domain necessary for loads analysis. The analysis time is limited to 1 h, and although this setup uses periodic boundary conditions, it takes more than one hour for the wind field to traverse through the very large parent domain, preventing the FWT on the inner domain from experiencing any large-scale structures more than once. Extensive analysis (not shown) revealed that when using a single domain with periodic boundary conditions, the FWT response in unstable and neutral BLs was strongly affected by the domain size. A spurious increase in FWT response was observed at low frequencies because of increased energy in the velocity field related to the periodicity of the single periodic domain. The nested domain setup describe above alleviated this issue.

For the stable BL, we use a single domain with a horizontal grid resolution of 8 m and periodic boundary conditions in the lateral directions, a time-step of 0.1 s, and a domain size of 4 km × 2 km. A nested setup is not necessary for the small turbulent structures in the stable BL, because the maximum size of stable BL structures is small enough that they are not affected by the domain size, in contrast to neutral and unstable conditions.

The turbulence intensity of the FINO-1 measurements at 81 m height and the LES at hub height is presented in Figure 1B. Figure 1C–E shows the shear profile of the LES generated wind fields compared to the profile obtained from the FINO-1 database. The shear profiles from LES match observations well, with shear increasing with stability; however, the turbulence intensities, especially for stable conditions, are generally lower than observations. This overall underprediction of TI is because the turbulent length scales in stable BLs are too small to be fully resolved on the current grid (and increased grid resolution is computationally prohibitive). The focus of the present work, however, is on the FWT response at lower frequencies, and these simulations resolve the necessary turbulent energy below approximately 0.2 Hz required for analysis.

2.4 | Synthetic wind generation models

The two synthetic turbulent wind models recommended by the design standards are the Kaimal spectral and exponential coherence model[5] and the Mann uniform shear model.[6,7] Both models are based on the Kaimal wind spectrum resulting in identical frequency content; however, the spatial distribution of the models differ, as further discussed in Sections 2.4.1 and 2.4.2. The effect of the two models on the responses of bottom fixed and onshore turbines has been seen to be similar, but for floating wind turbines, the responses are strongly affected by model selection.[9,11–13] The parameters of both models recommended in the standards are based on neutral atmospheric stability and on measurements that were not strictly offshore. In this work, we use two sets of parameters to generate the wind fields by the Kaimal and Mann models: The first set of parameters is fitted to the measurements from FINO-1, and the second set is fitted to the high-fidelity LES data. An alternative to these two synthetic models is to provide point measurements and use the TIMESR option in the TurbSim turbulence generator, as discussed in Section 2.4.3. The wind shear profile and turbulence intensity are the two common parameters for the three models.

2.4.1 | Wind profile fitting

There are two methods recommended by the IEC guidelines[4] to compute the wind shear profile: one based on a power-law and the other one on a logarithmic law. In the current work, we use the former to obtain the mean wind speed at hub height based on the FINO-1 measurements. The mean wind speed $\bar{u}$ at a certain height z using the power law is given by:

$$\bar{u}(z) = \bar{u}_{ref} \left(\frac{z}{z_{ref}} \right)^{\alpha}, \tag{2}$$

where $\bar{u}_{ref}$ is the wind speed at a reference height, z_{ref} is the reference height and α is the power-law exponent. The α exponent is defined as a bulk parameter that includes both the effect of surface roughness z_0 and atmospheric stability.[35,36] In this work, the wind speed at hub height is found by fitting the power law to the measurements from the cup anemometers at 34, 41, 51, 61, 71, 81, 91 and 101 m. Figure 1C–E shows the fitted wind profiles for the FINO-1 data measurements, indicated with squares, and for the LES data, indicated with stars. As shown through the shear exponents in Table 3, the shear decreases with decreasing stability; these values obtained are in agreement with previous studies.[37]

2.4.2 | Turbulence intensity

Turbulence intensity TI is defined as:

$$TI = \frac{\sigma_u}{\bar{u}_{hub}}, \tag{3}$$

where $\bar{u}_{hub}$ is the mean wind speed longitudinal component at hub height and σ_u the standard deviation of the same component. In the current work, for the models based on the FINO-1 measurements, the standard deviation is based on the measurements at 81 m: We assume that from this height up to the hub height the standard deviation remains constant. For the LES data, the standard deviation is computed at hub height. Figure 1B shows the computed turbulence intensity for both the FINO-1 measurements and for the LES data.

2.4.3 | Coherence

Another characteristic feature of the wind fields compared in this work is the spatial variation. A way to measure spatial variation is through the cross-spectra, which give information on the coherence of the specific processes between two points. Since it is a spectrum, it is composed of two parts: the real part (called co-coherence), which gives information on the frequency components, and the imaginary part (called quad-coherence), which provides information about the phases. Quad-coherence is present in the Mann model and the data from LES. The LES model accounts for quad-coherence in both lateral and vertical directions, whereas for the Mann model quad-coherence is only present in the vertical direction. The effect of stability on quad-coherence is negligible. However, for the low-frequency range, even though quad-coherence is lower than co-coherence, quad-coherence is non-negligible, and as Nybø et al[15] point out, quad-coherence leads to a phase shift that may have an impact on the dynamic response of offshore wind turbines. Kaimal and TIMESR do not present quad-coherence.

Magnitude-squared co-coherence (referred to as co-coherence or coherence γ hereafter) of two spatially separated processes i and j, as a function of frequency, is defined as:

$$\gamma_{i,j} = \frac{|C_{i,j}|^2}{P_i P_j}, \tag{4}$$

TABLE 3 Shear exponent α computed based on the FINO-1 measurements and LES data

Wind speed at HH [m/s]	Stable			Neutral			Unstable		
	7.5	12	16	7.5	12	16	7.5	12	16
α (fitted to FINO-1) [-]	0.057	0.142	0.173	0.050	0.082	0.073	0.049	0.059	0.052
α (fitted to LES) [-]	0.146	0.183	0.144	0.070	0.076	0.075	0.019	0.024	0.028

where P_i and P_j are the power spectra of the two time series separated by a specific lateral or vertical distance and $C_{i,j}$ is the cross spectrum between these two time series.

2.4.4 | Mann spectral tensor model (Mann)

The Mann uniform shear model is a spectral tensor-based turbulence model, which describes coherence in three dimensions. The spectral tensor uses conservation of momentum and mass to generate turbulence under neutral atmospheric conditions. The model has three parameters that are used to fit turbulence intensity and a specific turbulence spectrum: the non-dimensional shear distortion parameter Γ, the length scale parameter L, which describes the size of the energy-containing eddies, and the turbulent kinetic energy parameter $\alpha\epsilon^{2/3}$. To estimate the parameters based on the extracted wind speed measurements from FINO-1 at 81 m height, classified based on the atmospheric stability, and to the LES data at hub height, we use the Matlab function *fitMann* from Cheynet.[38] The spectra of the time series at 81 m are estimated using Welch's algorithm[39] with a Hamming window, six segments, and 50% overlapping, following previous works.[15,40] Then, the spectra are bin averaged before the fitting is performed. The resulting parameters fitted to both FINO-1 and LES, respectively, and for the nine scenarios, are presented in Figure 2. From Figure 2A, we see that L increases with decreasing stability, which is consistent with the larger eddies in unstable flows. Consistently with previous findings,[41] the shear distortion parameter Γ fitted to the FINO-1 measurements generally increases with decreasing stability. The Γ parameter fitted to LES data shows an opposite trend, i.e. it decreases as stability decreases; however, de Maré et al[16] found the same. The energy dissipation rate parameter $\alpha\epsilon^{2/3}$ is expected to increase with decreasing stability. For the LES fitting, this is seen to hold. The trend of the parameter fitted to the FINO-1 measurements differs from this hypothesis: for the rated and over-rated scenarios, the highest value is seen for the neutral case. Nevertheless, this trend is consistent with the wind spectra in Figure 4, where the neutral and unstable measurements present similar energy levels at high frequencies at the rated and above-rated scenarios.

Coherence $\gamma_{i,jK}(k,\delta)$ is inherent to the Mann model; i and j are the two time series separated by distance δ, k is the wave number and $K = u,v,w$ indicates the specific velocity component. Coherence is given by the integral of the spectral tensor $\phi_{i,j}$ itself, which depends on the lateral and vertical separation distances, δ_y and δ_z, and the spatial lateral and vertical wave numbers k_y and k_z:

$$\gamma_{i,jK}(k,\delta) = \frac{|\int\int \phi_{i,j}dk_ydk_z e^{-ik_y\delta_y}dk_ydk_z e^{-ik_z\delta_z}dk_ydk_z|^2}{\int\int \phi_{i,i}dk_ydk_z \int\int \phi_{j,j}dk_ydk_z}. \tag{5}$$

2.4.5 | Kaimal spectrum and exponential coherence model (Kaimal)

The Kaimal spectrum with exponential coherence model is based on the Kaimal spectrum in the three components. Coherence is not intrinsic to this model, and therefore, it is generally added to the generated points by the following exponential function:
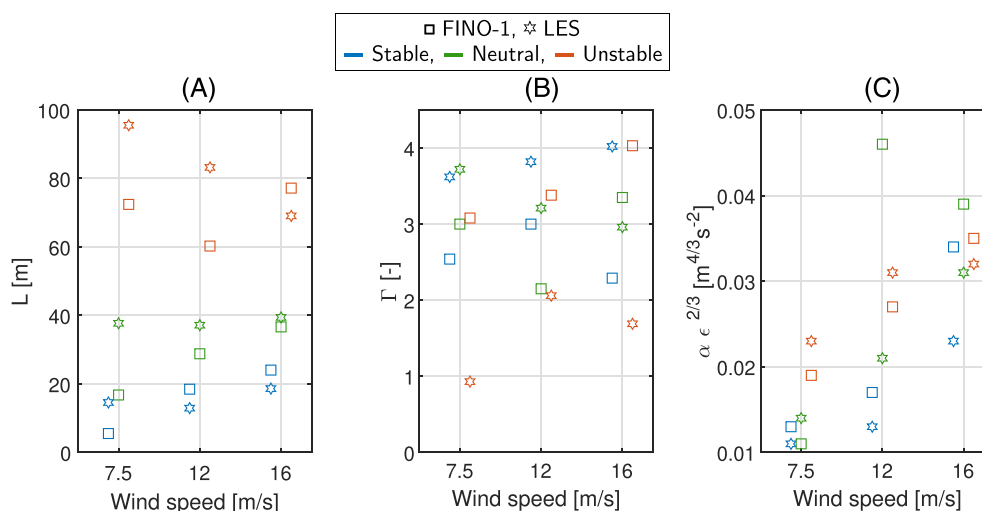

FIGURE 2 Mann model parameters fitted to the FINO-1 measurements and to the LES data for the three mean wind speeds and stable, neutral and unstable atmospheric conditions. (A) Length scale parameter L, (B) shear distortion parameter Γ and (C) energy dissipation rate parameter $\alpha\epsilon^{2/3}$

TABLE 4 Coherence parameters a_K and b_K of the Kaimal model and Davenport coherence model parameters C_K

	Stable			Neutral			Unstable		
	7.5 m/s	12 m/s	16 m/s	7.5 m/s	12 m/s	16 m/s	7.5 m/s	12 m/s	16 m/s
Fitted to FINO-1 measurements									
a_u	12.00	7.77	16.10	4.24	5.77	7.39	2.59	4.71	7.48
b_u	$-3.39\cdot10^{-7}$	$6.99\cdot10^{-4}$	$4.33\cdot10^{-4}$	$4.02\cdot10^{-7}$	$1.78\cdot10^{-3}$	$2.84\cdot10^{-4}$	$-1.93\cdot10^{-6}$	$2.11\cdot10^{-7}$	$-5.02\cdot10^{-7}$
a_v	13.00	3.46	4.95	3.42	14.80	3.65	1.70	3.15	4.26
b_v	$-1.48\cdot10^{-7}$	$2.84\cdot10^{-3}$	$3.81\cdot10^{-3}$	$5.35\cdot10^{-4}$	$9.31\cdot10^{-9}$	$2.57\cdot10^{-3}$	$-3.21\cdot10^{-5}$	$3.83\cdot10^{-4}$	$1.32\cdot10^{-3}$
a_w	2.52	3.03	4.33	2.33	3.10	2.90	1.16	1.93	3.26
b_w	$6.60\cdot10^{-3}$	$6.00\cdot10^{-3}$	$5.89\cdot10^{-3}$	$5.35\cdot10^{-3}$	$3.31\cdot10^{-3}$	$4.32\cdot10^{-3}$	$5.93\cdot10^{-3}$	$2.25\cdot10^{-3}$	$2.16\cdot10^{-3}$
C_u	21.24	17.05	38.71	8.51	17.78	15.10	4.88	8.86	14.37
C_v	28.37	9.92	40.75	6.92	30.05	9.63	3.40	6.35	10.11
C_w	10.39	19.08	75.33	7.19	8.91	11.71	2.78	4.25	8.13
Fitted to LES data									
a_u	1.90	3.32	4.15	1.27	2.64	4.15	1.47	2.55	3.15
b_u	$-2.09\cdot10^{-3}$	$-1.39\cdot10^{-4}$	$7.02\cdot10^{-4}$	$-1.06\cdot10^{-3}$	$5.61\cdot10^{-4}$	$3.63\cdot10^{-5}$	$2.49\cdot10^{-6}$	$7.37\cdot10^{-7}$	$3.59\cdot10^{-4}$
a_v	0.46	1.58	1.99	0.97	1.64	2.32	1.10	1.65	2.24
b_v	0.04	0.02	0.01	$7.74\cdot10^{-3}$	$3.71\cdot10^{-3}$	$2.98\cdot10^{-3}$	$-1.80\cdot10^{-3}$	$2.02\cdot10^{-3}$	$7.64\cdot10^{-4}$
a_w	0.75	1.31	1.44	0.56	0.92	1.18	0.46	0.82	1.00
b_w	0.01	$7.99\cdot10^{-3}$	$7.64\cdot10^{-4}$	$3.87\cdot10^{-4}$	$5.23\cdot10^{-3}$	$3.39\cdot10^{-3}$	$-1.8\cdot10^{-3}$	$-1.4\cdot10^{-3}$	$2.03\cdot10^{-3}$
C_u	4.95	3.43	3.14	10.00	6.47	5.74	12.49	18.83	6.16
C_v	7.66	2.76	2.40	17.22	4.75	4.00	18.83	7.30	6.35
C_w	2.23	1.25	0.95	4.58	2.40	1.77	6.16	3.46	2.36

$$\gamma_{i,j}(\delta,f) = \left[\exp\left(-a_K \sqrt{\left(\frac{f\delta}{\bar{u}_{hub}}\right)^2 + (\delta b_K)^2} \right) \right]^2, \tag{6}$$

where δ is the separation distance between time series i and j of the K component, f is the frequency in Hertz, a_K the coherence decrement parameter and b_K the coherent offset parameter. In the current work, the coherence parameters for the Kaimal model are obtained by fitting Equation (6) to both the FINO-1 measurements and the LES data, separately for the two sets of comparisons. For the FINO-1 measurements, δ is given by the distance between the ultrasonic anemometers, i.e., 20 m. For the LES data, δ is 24 m. Table 4 shows the coherence parameters a_K and b_K for the nine scenarios, for both the FINO-1 and the LES fitted models.

2.4.6 | TIMESR

An alternative to generate wind fields in the TurbSim turbulence generator is to provide measurements of the wind speed components at specific points. Based on the input time series, the spectral amplitudes are computed and linearly interpolated. Two sets of point measurements and data, respectively, are used in the current work: The first is based on the FINO-1 measurements, and the second is based on the LES data. We use time series placed at three different heights: The FINO-1 measurements are at 41, 61 and 81 m, and the data used from LES are placed at 120, 136 and 152 m. Even though the LES data are available for 870 points distributed vertical and horizontally, we decide to use three vertically distributed points as input to generate the wind fields with TIMESR, so that the comparison between the models fitted to FINO-1 point measurements and LES data is more consistent. To ensure coherence once the time series are generated based on the Veers' method,[42] the phases are modified using a coherence function. In the current work, the Davenport coherence model is used. This coherence model is based on describing the longitudinal turbulence component for different vertical separations by an exponential function with a decay parameter, C_K, as follows:

$$\gamma_i(\delta,f) = \exp\left(-C_K \frac{f\delta}{\bar{u}_{hub}} \right). \tag{7}$$

Previous works from Cheynet et al[40] and Nybø et al[15] show that the Davenport model fits well the u- and v-coherence of the FINO-1 measurements. Therefore, based on these findings, we use the same coherence model to fit the FINO-1 point measurements and the LES data. The fitted exponential parameters C_u, C_v and C_w for every scenario are presented in Table 4.

2.4.7 | Wind field generation and coherence

To generate the wind fields based on the Kaimal and TIMESR models, TurbSim[21] is used. The wind fields generated based on the Mann model are generated in the IEC 64bit turbulence generator.[43] Both the Kaimal and Mann models use Taylor's hypothesis of frozen turbulence. The Kaimal model produces time-dependent wind in 2D planes and uses Taylor's hypothesis to extend it into a third dimension. The Mann model generates a three-dimensional static wind box and Taylor's hypothesis is applied to move this wind box along the domain in the longitudinal direction. The wind fields generated by LES are directly used as input to OpenFAST by converting the time series from the data point files to a consistent format (.bts).

The Kaimal, Mann and TIMESR models have 32 points in z and y and 65,536 (2^{16}) in x. The height and width of the turbulence box is 249.36 m, with the hub at the middle of the grid. The base of the grid lies at 7.02 m and goes up to 256.38 m high. The resolution in both y and z directions is 8.04 m. In the x direction, the grid resolution depends on the mean wind speed at the reference height of the grid. For the three cases evaluated in the current work, dx varies from 0.46 to 0.98 m. The time step of the simulated wind field is equal to $T/N_x = 0.06$ s, based on Taylor's frozen turbulence hypothesis, where T is the duration of the wind field and N_x the number of points of the wind field in the x direction. The wind fields generated by LES start at 16 m above the ground and extend up to 248 m. There are 29 points in y, 30 points in z and 36,000 in x. The resolution in y and z is 8.00 m and the model time step is 0.1 s. For each scenario and model, six turbulent wind fields of 1-h duration are generated.

Robertson et al[44] demonstrated the importance of the lateral coherence of the longitudinal wind speed component in the Kaimal model for the structural loads of a bottom-fixed turbine. Figure 3 shows the u-component lateral coherence for the nine scenarios and the three models fitted to the LES data, and for the LES data themselves, for a distance δ_y of 0.5 and 1 rotor diameter (D), as a function of the reduced frequency ($f_r = f\delta_y/U_w$). The lateral coherence for the models fitted to the FINO-1 measurements is not shown here because the comparison between the models and conditions presented in the following applies. In general, lateral coherence decreases as the separation distance increases, and tends to zero as frequency increases. Both the Kaimal and Mann model present higher coherence for unstable conditions. For the LES data, higher
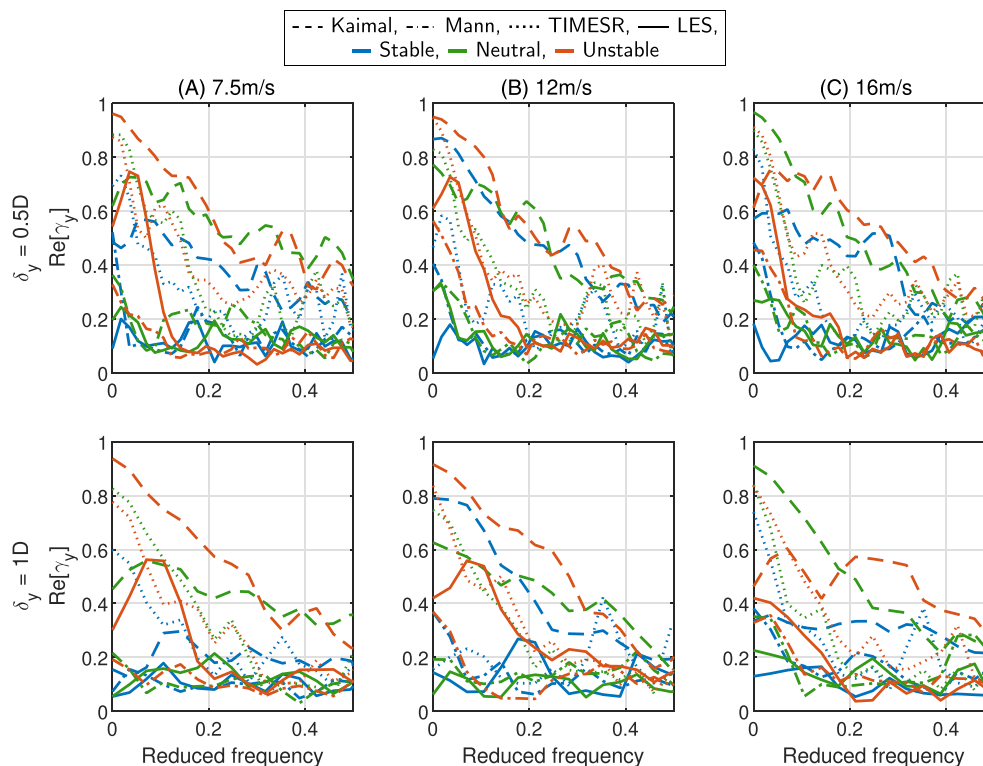

FIGURE 3 Lateral coherence of the longitudinal velocity component as a function of the reduced frequency for the models fitted to the LES data for δy = 0.5D and 1D, top and bottom, respectively, and for 7.5 m/s (A), 12 m/s (B) and 16 m/s (C)
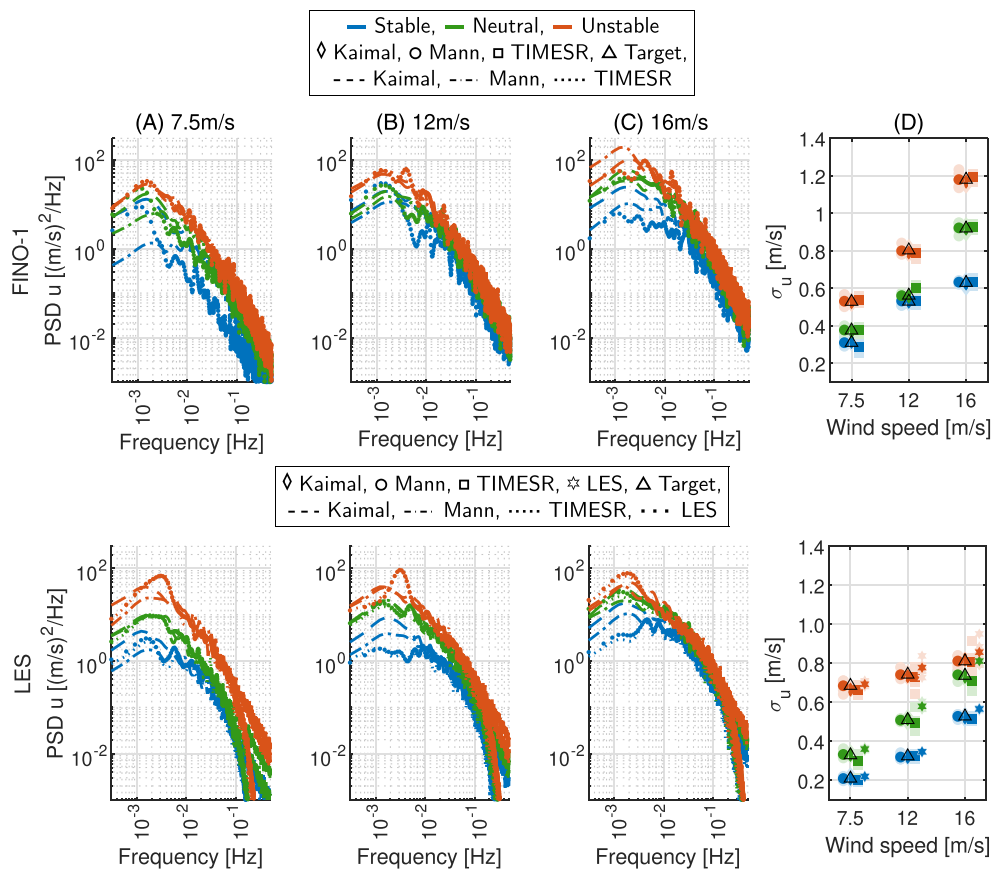
FIGURE 4 (A–C) PSD of the u-velocity component at hub height for each of the wind turbulence generation methods for the mean wind speeds of 7.5 m/s (left), 12 m/s (middle) and 16 m/s (right). (D) Average of the six seeds of the standard deviations of the grid points over the rotor area of the u-component of the wind speed for each condition and wind model. The top row corresponds to the models fitted to FINO-1 measurements, and the bottom row to the ones fitted to the LES data

coherence for the unstable and neutral cases is also seen. The largest coherence under unstable conditions for the lowest frequencies, or wave numbers, is consistent with the larger eddy size as stability in the atmosphere decreases. The TIMESR model fitted both to the LES data and to the FINO-1 measurements presents the same trend: higher coherence under unstable conditions for lower wave numbers. The Kaimal model shows in general the highest coherence, followed by the TIMESR and LES models; the Mann model is seen to have the lowest coherence, regardless of the stability condition or lateral distance.

Figure 4A–C, top, presents the power spectral density (PSD) of the longitudinal velocity component at hub height for the three wind models fitted to the FINO-1 measurements, and for the three mean wind speeds at hub height. Figure 4D shows the average of the standard deviation of the longitudinal component of every grid point across the rotor area for the six seeds in lighter coloured symbols. The solid symbols represent the average of the six realisations. Figure 4, bottom, shows the same as the top figures, but for the Kaimal, Mann and TIMESR models fitted to the LES data, together with the LES data themselves. The energy content of the longitudinal velocity for the TIMESR model and the LES data decreases for frequencies above approximately 0.1 to 0.2 Hz due to the grid resolution, whereas Mann and Kaimal continue to cascade at the −5/3 power law. Nevertheless, the scope of the present work is to study the response of the FWT structure at lower frequencies than 0.2 Hz.

The average standard deviations of the wind fields from the Kaimal, Mann and TIMESR models are seen to be very close to the respective target values, represented by a triangle. The target values are based on the FINO-1 measurements at 81 m and on the LES data at hub height, consistently with the TI shown in Figure 1B. The standard deviation of the LES wind fields is slightly higher than the target value because the target value was computed for hub height, not as an average, while the results are presented as averages of all the points across the rotor. Therefore, a larger spread of the wind speed, and a slight deviation from the target, is expected. The wind fields generated by LES present a resonance at 0.003 Hz for the 7.5 and 12 m/s scenarios, and at 0.0018 Hz for the 16 ms case, under unstable conditions. The higher energy content at those two frequencies, respectively, is related to a characteristic size of the convective cellular structures resolved in the LES data[45]; this higher energy content at these frequencies is captured by the TIMESR model, but not by the Mann and Kaimal models. The characteristic size for a frequency of 0.003 Hz is related to eddies of 2,500 and 4,000 m long, respectively for the 7.5 and 12 m/s cases. The TIMESR model fitted to the FINO-1 measurements also presents higher energy content at around 0.003 Hz under unstable conditions, for the three wind speed scenarios. Similar to the

LES data, this higher energy content is likely to be related to a characteristic wavelength or size of convective cellular structures in unstable conditions as seen in observations offshore.[46]

2.5 | Fatigue analysis

To assess fatigue loading, we use the short-term damage equivalent loads (DEL^{ST}), which are computed using the MLife Matlab scripts[47,48] developed at NREL. The DEL^{ST} for a time series j of 3,600 s (after 500 s transient) duration is formulated in the current work as:

$$DEL_j^{ST} = \left(\frac{\sum_i (n_{ji}(L_{ji}^R)^m)}{n_j^{STeq}} \right)^{1/m},$$ (8)

where n_{ji} is the ith cycle count, m is the Wöhler exponent, equal to 3 for the steel tower and mooring lines, and equal to 10 for the blades, and L_{ji}^R is the cycle's load range without using Goodman's correction. n_j^{STeq} is the total equivalent fatigue counts, such that the fatigue load that yields the equivalent damage is:

$$D_j^{ST} = \sum_i \frac{n_{ji}}{N_{ji}} = \frac{n_j^{STeq}}{N_j^{eq}},$$ (9)

where N_{ij} is the number of cycles to failure and N_j^{eq} is the equivalent number of cycles until failure. In this work, the equivalent frequency is 1 Hz. Furthermore, a low-pass filter of 0.1 Hz is applied to the time series when computing the DEL, to eliminate wave-frequency effects when comparing the wind models and atmospheric stability conditions.

3 | INO WINDMOOR 12MW FWT

The floating wind turbine model used to study the effect of atmospheric stability and the two sets of wind field generation models is the INO WINDMOOR 12MW floating wind turbine, shown in Figure 5, left. The platform is a semisubmersible, with three columns connected by three
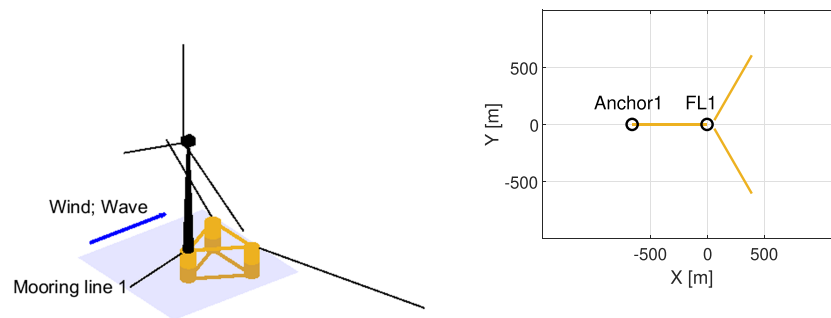

FIGURE 5 Left: geometry of the INO WINDMOOR 12MW model. Right: layout of the mooring system

TABLE 5 INO WINDMOOR 12MW main characteristics

Water depth [m]	150
Draft [m]	15.5
Displacement [t]	1416
Centre of gravity [m]	-9.7
Platform roll, pitch & yaw inertia about SWL [t m^2]	$6.703 \cdot 10^6, 4.1559 \cdot 10^6$ and $9.4548 \cdot 10^6$

TABLE 6 INO WINDMOOR 12MW wind turbine main characteristics

Rotor diameter	Cut-in, rated, cut-out wind speed	Cut-in, rated rotor speed
216.9 m	4 m/s, 11.4 m/s, 25 m/s	5.5 rpm, 7.8 rpm

TABLE 7 Platform's natural frequencies in OpenFAST

Degree of freedom	Surge	Sway	Heave	Roll	Pitch	Yaw	1P	1st FAB
Frequency [Hz]	0.011	0.011	0.062	0.035	0.033	0.013	0.130	0.641

Abbreviations: FAB, tower fore-aft bending frequency; 1P, rated rotor frequency.

upper and three bottom pontoons. The tower is installed on top of one of the columns. The mooring system consists of three hybrid (chain and polyester) catenary mooring lines; the layout is shown in Figure 5, right. The fairleads (FL) are at the still water level ($z = 0$), with a pretension of 1,050 kN. Tables 5 and 6 present the main features of the platform and the wind turbine,[19] respectively.

The main characteristics of each of the segments of the mooring lines are provided in the work of de Souza et al.[19] The model in OpenFAST 2.5.0 is built based on the model previously built in SIMO-RIFLEX,[49] an aero-hydro-servo-elastic tool from SINTEF Ocean. The frequencies of the six rigid modes of the platform, together with the 1P rotating frequency at rated wind speed and the first tower fore-aft bending frequency are given in Table 7.

4 | RESULTS AND DISCUSSION

In this section, we show the standard deviation of surge, pitch and yaw to study the effect of the wind generation models and stability conditions on these global motions. Heave, sway and roll are not presented here because motions for these degrees of freedom under the given conditions are relatively small. As for the load response, previous studies have shown that the wind field modelling and the stability conditions applied affect the loading on the tower, the blades and the mooring lines. Therefore, we focus on the standard deviation and short-term DEL of the base fore-aft bending moment (TBFABM), the tower top torsional moment at the yaw bearing (TTYBM), the blade root out-of-plane moment (BROoPM) and the tension at the FL 1, i.e., at the upwind position as indicated in Figure 5.

4.1 | Models fitted to FINO-1 point measurements

Figure 6, top, shows the mean of the standard deviation for the six seeds in surge, pitch and yaw for the three mean wind speeds at hub height, the three atmospheric stability conditions and for the Kaimal, Mann and TIMESR models fitted to the FINO-1 measurements. The motions under unstable atmospheric conditions are the largest, as expected, due to a higher turbulence intensity. For the stable and neutral cases, the response is very similar. Lateral coherence is higher under unstable conditions, which contributes to the higher standard deviation of surge and pitch. The larger coherence together with a higher TI under unstable conditions explains the larger response for surge and pitch. In the case of yaw, the higher response under unstable conditions is explained by the higher TI. TIMESR and Kaimal show higher coherence, and consequently, the standard deviation in pitch and surge is, in general, between 11% and 20% higher than the one observed for the Mann model. For the Mann model, the standard deviation in yaw is around 25% higher than for the Kaimal and TIMESR models. The larger response for the Mann model in yaw is particularly prominent close to the natural frequencies in surge and yaw (f_1 and f_6 in Figure 6) under unstable conditions. Surge is also excited at its natural frequency f_1, at around 0.011 Hz, and the highest energy content is observed for the Kaimal model, which is consistent with the higher standard deviation that the Kaimal model shows in surge. The contribution of the waves at higher frequencies is negligible compared to those of the wind at the frequency range below 0.3 Hz. The largest response in surge and pitch is observed for the case at rated wind speed, whereas the standard deviation in yaw increases as so does wind speed. Furthermore, for the TIMESR model, for pitch and surge, there is a higher energy content at the same frequency (0.003 Hz) as previously mentioned for the wind fields PSD (Section 2.4.4), related to the size of convective cellular structures. The findings on the global motions presented here coincide with the ones from Nybø et al,[17] where the pitch and surge standard deviations for the TIMESR and Kaimal models are found higher compared to the ones from the Mann model, and the opposite is found for the yaw standard deviation.

Figure 7, top, presents the standard deviation of the TBFABM, the TTYBM and the BROoPM for the three mean wind speeds at hub height, the three models (Kaimal, Mann and TIMESR) and the three atmospheric stability conditions. The standard deviation of the TBFABM is correlated with the pitch standard deviation. The response is the highest under unstable conditions, and in general between 12% and 16% lower for Mann
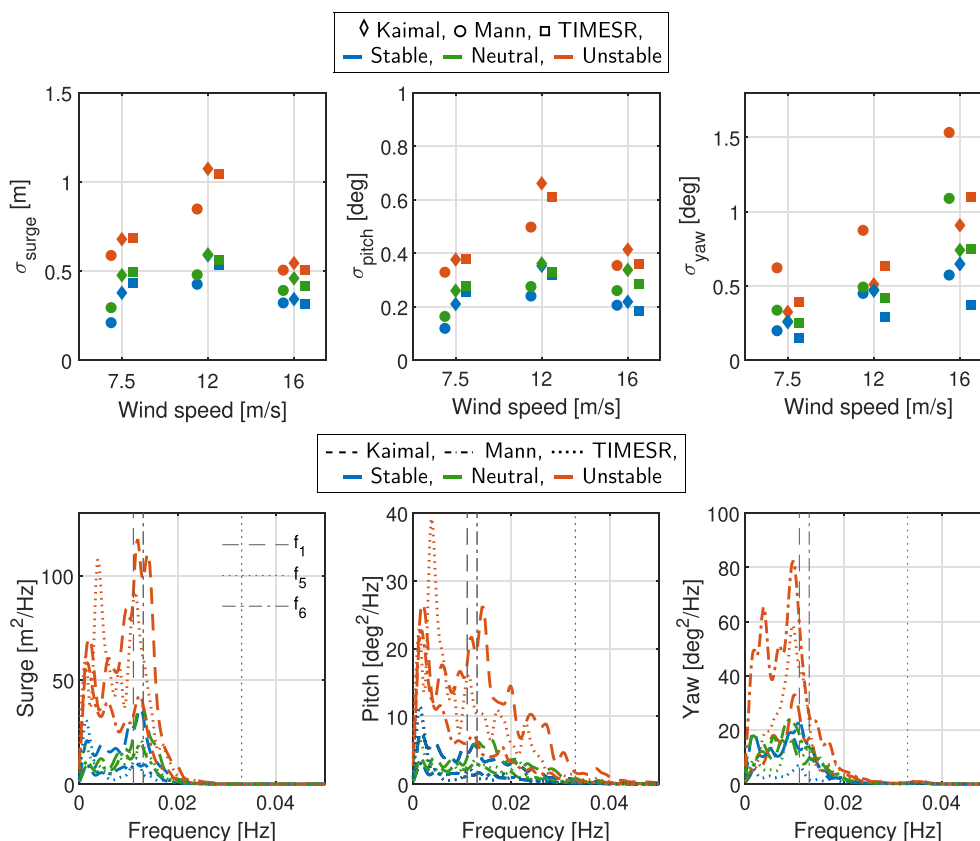
FIGURE 6 Top: average of the standard deviation of surge, pitch and yaw, for the six seeds, for the models fitted to the FINO-1 measurements. Bottom: average of the six seeds of the PSD of the motions for the 12 m/s scenario. f_1, f_5 and f_6 are the surge, pitch and yaw natural frequencies, respectively

compared to TIMESR and Kaimal, regardless of the stability condition. The TBFABM standard deviation is affected by the wave height, as seen from the PSD of the TBFABM for 16 m/s in Figure 7, bottom. Nevertheless, the wave conditions are the same for every stability condition, and therefore, the comparison between models and stability conditions is not affected. This observation is supported by the DEL for the TBFABM, in Figure 9, for which, as already mentioned, a low-pass filter of 0.1 Hz is applied. The standard deviation of the TTYBM is directly correlated to the standard deviation in yaw. For the Kaimal and TIMESR models, the lateral coherence is higher, and therefore the TTYBM standard deviation is, in general, between 20% and 30% lower. The response for the Mann model, under unstable conditions, is the largest. The blade-passing, or 3P, and the 1P frequencies affect the response under stable conditions due to shear. This effect is more noticeable as the rotor speed becomes more steady, as is the case for the 16 m/s scenario, on both the PSD of the TTYBM and BROoPM (Figure 7, bottom), and the standard deviation of the BROoPM (Figure 7, top right).

Figure 8 presents the standard deviation and PSD of the tension at fairlead 1 (FL1) for the three wind speed scenarios, the three models and the three stability conditions. The results show a very high correlation with the surge and pitch motions, not only for the standard deviation but also for the PSD. Neither the model nor the atmospheric stability show a large influence on the response, except for the scenario where the wind speed is close to rated, i.e., 12 m/s. For this case, the tension under unstable conditions is 25% larger than the one under neutral conditions, due to a higher turbulence intensity and higher coherence. Furthermore, the difference between the models is more evident under this scenario, which implies that coherence has a larger effect. The fairlead tension is lower for the Mann model, which is explained by the lower coherence of this model. At lower frequencies, the response for the TIMESR model under unstable conditions shows three peaks at 0.0018 Hz, 0.0036 Hz (which was mentioned in Section 2.4.4) and 0.0112 Hz. The latter frequency coincides with the surge natural frequency, which is equally captured by the Kaimal and Mann models.

Figure 9 shows the short-term damage equivalent (DEL) loading for the TBFABM, the TTYBM, the BROoPM and the FL 1 tension, for the three stability conditions and the three mean wind speed scenarios for the models fitted to FINO-1 measurements. A very similar trend to the standard deviation of the responses is observed: for the TBFABM DEL, unstable conditions show the largest response, followed by the neutral and stable conditions. The Kaimal model responses overestimate the loading compared to TIMESR, whereas the Mann model responses underestimate it, due to its lower coherence. For the TTYBM DEL, the loading is governed by the lateral coherence of the models: The TTYBM DEL of
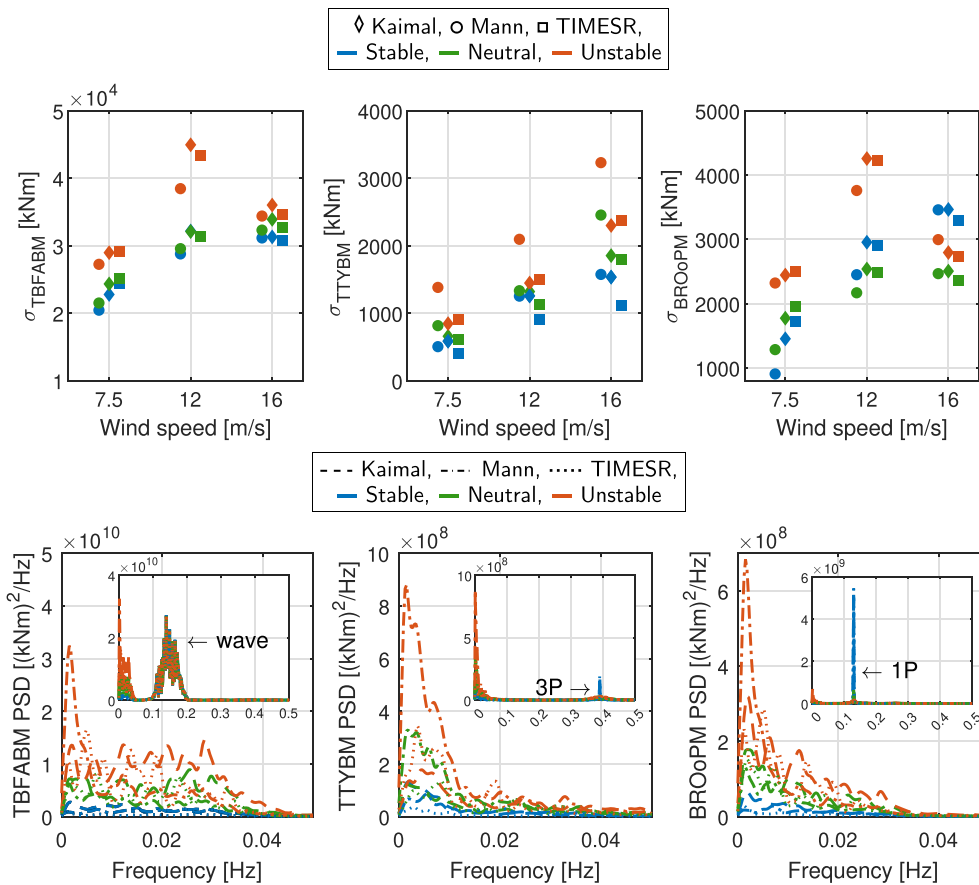
FIGURE 7   Top: average of the standard deviation of the tower base fore-aft bending moment, the torsional yaw bearing moment at the rotor base and the blade root out-of-plane moment, for the six seeds, for the models fitted to the FINO-1 measurements. Bottom: average of the six seeds of the PSD of the structural response for the 16 m/s scenario
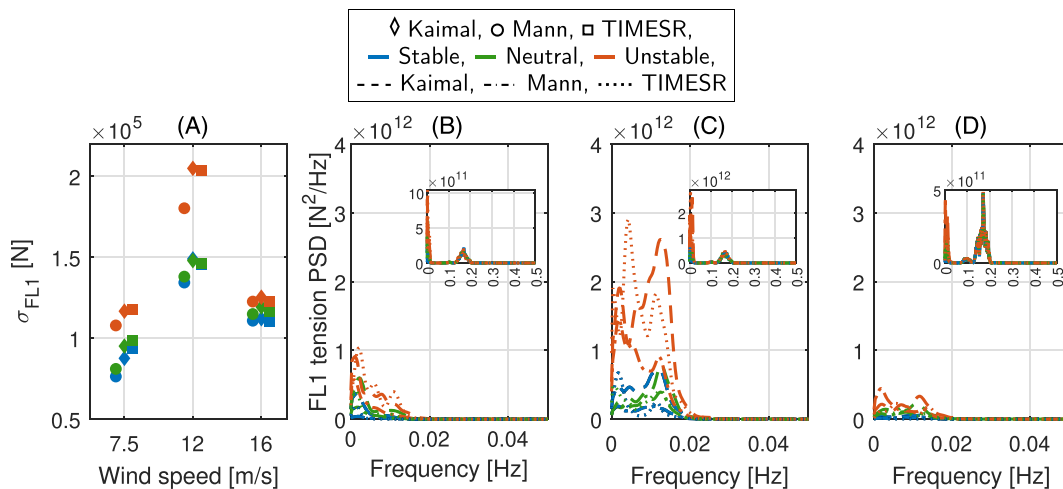

FIGURE 8   (A) Average of the standard deviation, for the six seeds, of the tension at fairlead 1, placed upwind. (B–D) Average PSD for the six seeds of the tension at the fairlead for 7.5, 12 and 16 m/s, respectively. These results correspond to the models fitted to the FINO-1 measurements

the Kaimal model is very similar to the TIMESR model for neutral and unstable conditions. The TTYBM predicted by the Mann model is the highest one, which is explained by the lower coherence of this model. Doubrawa et al,[9] who studied the response for a spar-type FWT, also found that under neutral conditions the tower base yaw DEL was higher for the Mann than for the Kaimal model. The BROoPM DEL is highest under
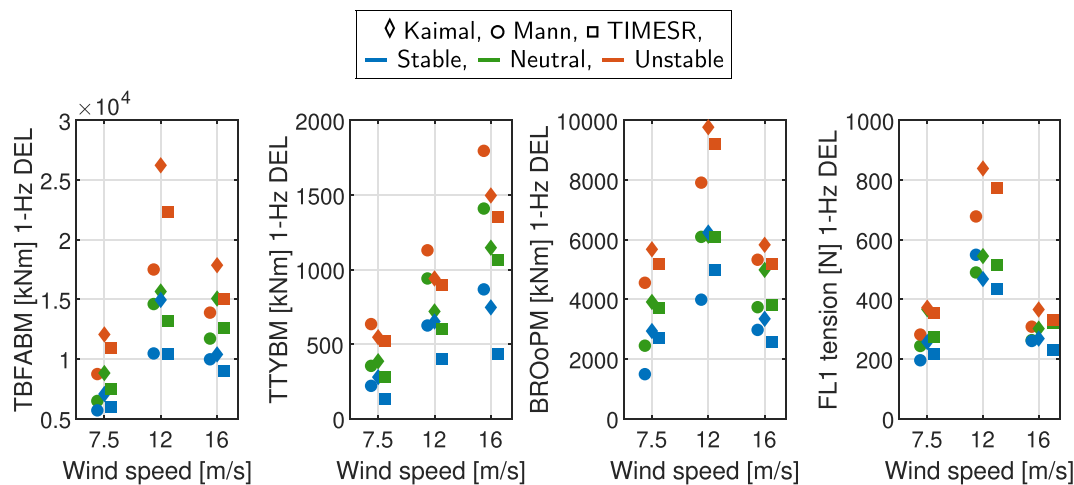
FIGURE 9 Short-term DEL for the TBFABM, TTYBM, BROoPM and FL1 tension, for the models fitted to the FINO-1 measurements
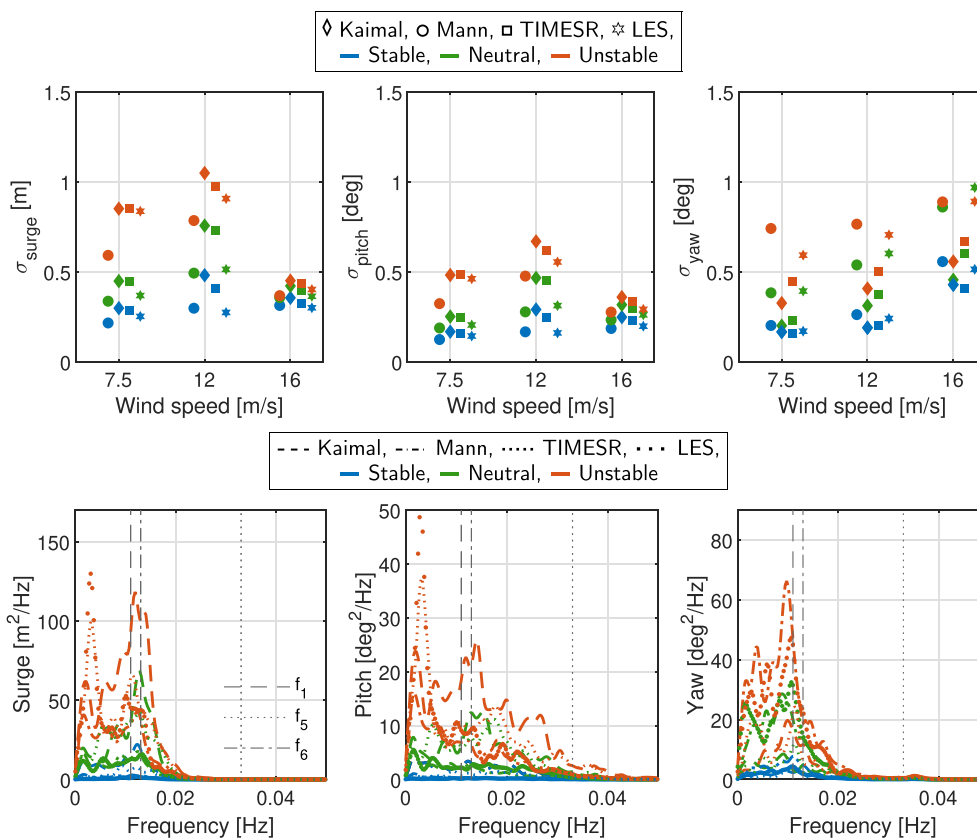

FIGURE 10 Top: average of the standard deviation of surge, pitch and yaw, for the six seeds, for the models fitted to the LES data. Bottom: average of the six seeds of the PSD of the motions for the 12 m/s scenario. f_1, f_5 and f_6 are the surge, pitch and yaw natural frequencies, respectively

unstable conditions for every scenario, since the frequencies over 0.1 Hz have been filtered; otherwise, as it is seen from the standard deviation of the BROoPM, stable conditions would show a larger DEL for the over-rated scenario, due to a higher shear. The Kaimal and TIMESR models show very similar values, and higher than the Mann model, in general. Doubrawa et al[9] found that for the over-rated wind speed scenario, the Kaimal model yielded higher DEL than the Mann model, whereas for the rated wind speed scenario the Mann and Kaimal models showed very similar values. These findings for these two scenarios are in line with what it is observed in this work. The FL1 tension DEL shows a higher loading for unstable conditions for the Kaimal and TIMESR models compared to the Mann model, especially for the rated wind-speed scenario. For this

scenario, at 12 m/s, and especially for unstable and neutral conditions, these findings for the fairlead tension are consistent with the work from Nybø et al,[17] even though their work focused on a spar-type FWT. Under neutral and stable conditions, for the below- and over-rated scenarios, the Kaimal, Mann and TIMESR models yield very similar responses. Bachynski and Eliassen[12] observed the same trend for neutral conditions, for below- and over-rated scenarios, for a semisubmersible structure.

4.2 | Models fitted to LES data

Figure 10, top, shows the standard deviation in surge, pitch and yaw for the three mean wind speeds at hub height, the three atmospheric stability conditions and the three models fitted to the LES data (Kaimal, Mann and TIMESR) and the LES data themselves. Similarly to what we observe for the response for the models fitted to the FINO-1 measurements, the response in surge, pitch and yaw under unstable atmospheric conditions is the largest, regardless of the model. For the LES data, we observe that the difference in standard deviation in yaw between neutral and unstable conditions is smaller for the 12 m/s scenario compared to the 7.5 m/s; for the 16 m/s case the neutral condition shows a larger standard deviation. This higher yaw under neutral conditions for the 16 m/s scenario is explained by a lower coherence under neutral conditions, and a larger difference in coherence with the unstable scenario (see Figure 3). For the 7.5 m/s and the 12 m/s scenarios, the higher TI for unstable conditions dominates; however, for the 16 m/s, the effect of the difference in coherence is larger than the difference in TI. Therefore, for the 16 m/s scenario, under neutral conditions, the effect of a higher coherence in the response compensates for the effect of a lower TI.

The trend of the models fitted to the LES data is very similar to the one seen for the models fitted to the FINO-1 data. Compared to the LES data, the Mann model underestimates surge and pitch motions, especially under unstable conditions. On the contrary, TIMESR and Kaimal overestimate surge and pitch motions. For neutral and stable conditions, for the 7.5 m/s and 16 m/s scenarios, the maximum under- or overestimation of the models with respect to the LES data is of 12%. Yaw is well predicted by the Mann model, and underpredicted by the TIMESR and Kaimal models. The under- and overprediction of the PSD of the motions for the different models is seen to drive the standard deviation. Similarly to what we observe for the TIMESR model fitted to the FINO-1 measurements, from the PSD of surge and pitch of the 12 m/s scenario
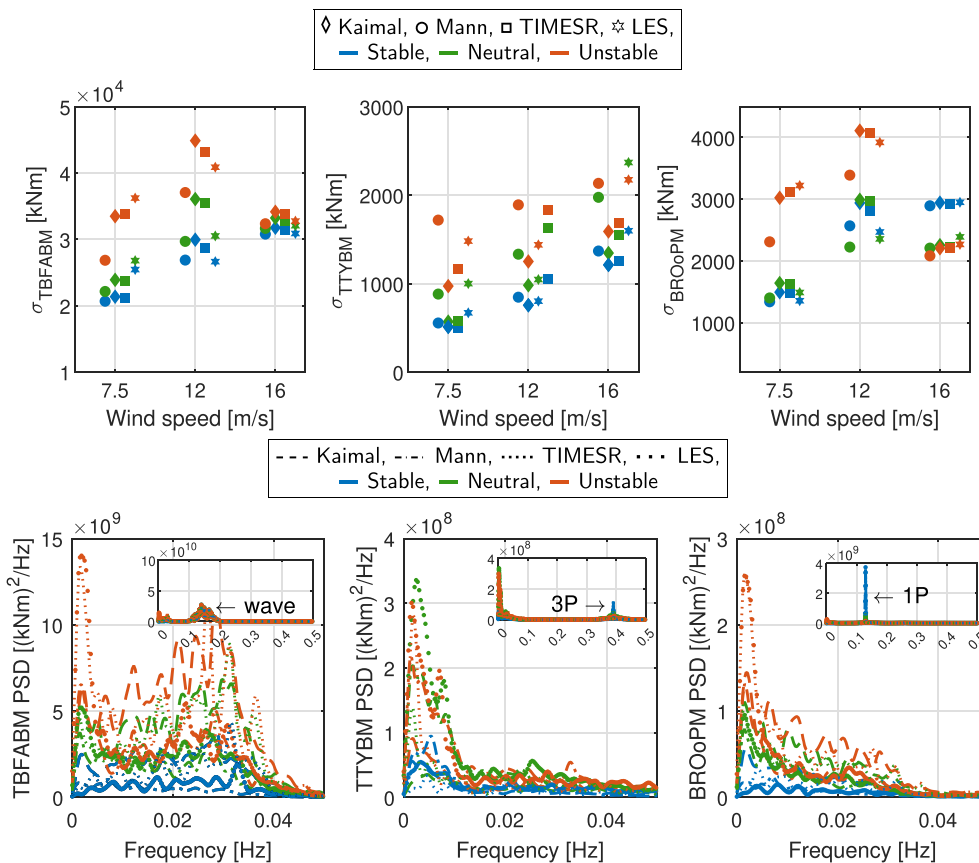

FIGURE 11 Top: average of the standard deviation, for the six seeds, of the TBFABM, the TTYBM and the BROoPM, for the models fitted to the LES data. Bottom: average of the six seeds of the PSD of the structural response for the 16 m/s scenario

(Figure 10, bottom), the higher energy content at around 0.003 Hz is captured by the TIMESR model, but not by the Kaimal and Mann models. Nybø et al[17] found that the surge and pitch standard deviation of the LES model was lower than the Kaimal, TIMESR and Mann models, under neutral conditions, for the cases at and over-rated wind speeds. When comparing stability conditions at rated wind speed, they also found that under unstable conditions the standard deviation of the LES is very similar to the Kaimal and TIMESR models.

Figure 11, top, presents the standard deviation of the TBFABM, the TTYBM and the BROoPM for the three mean wind speeds, for the Kaimal, Mann and TIMESR models and the LES data and the three atmospheric stability conditions. The trends for the Kaimal, Mann and TIMESR models are very similar to the ones observed for the response of the models fitted to the FINO-1 measurements. The model fitted to the LES data shows a different trend for the TTYBM for 16 m/s under unstable conditions: in this case the highest response is seen for neutral conditions, instead of under unstable ones. The reason is the same as for the highest yaw standard deviation under the same conditions: coherence for neutral conditions is lower, and its difference with the coherence for unstable conditions is higher than for the other models. Figure 11, bottom, shows the PSD of the response for the 16 m/s wind speed scenario. From the PSD of the TTYBM, it can be seen the higher response under
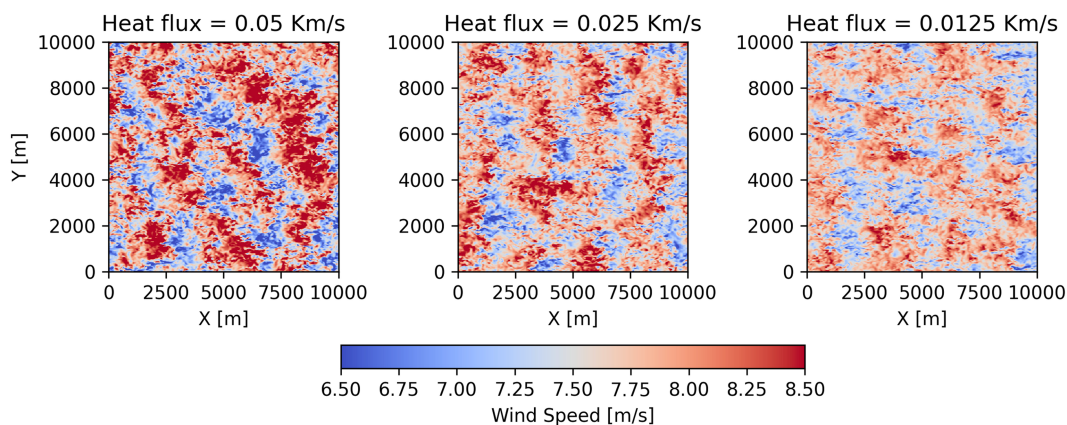

FIGURE 12 Hub height wind speed for the three heat flux rate cases in the parent domain, applied to the 7.5 m/s scenario
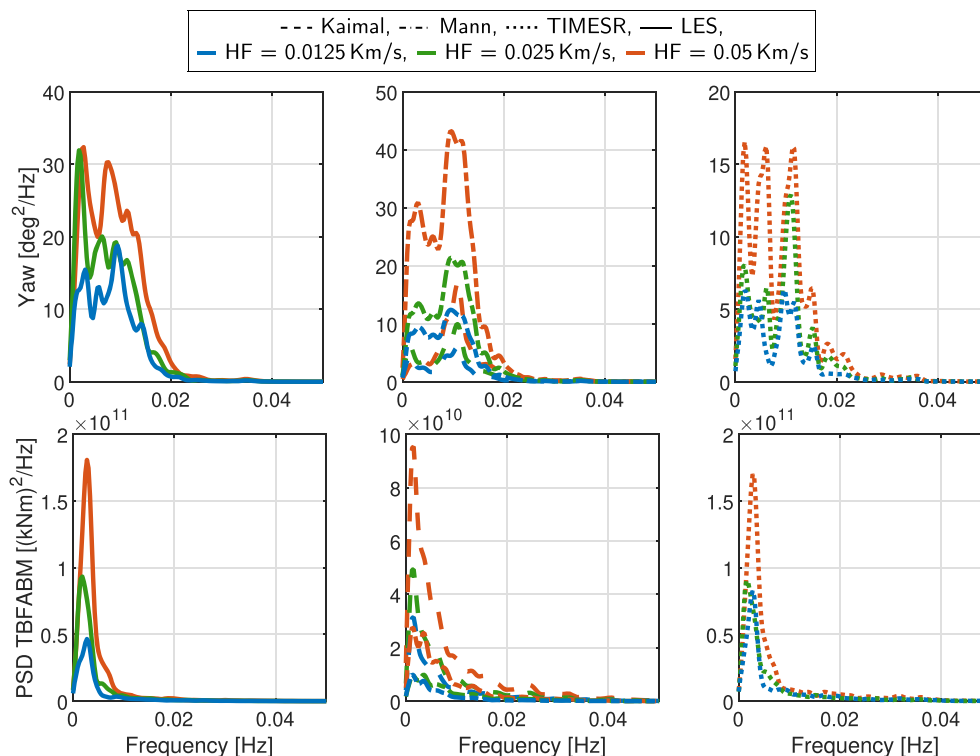

FIGURE 13 Top: PSD of yaw for the LES data (left) Kaimal and Mann (middle) and TIMESR (right). Bottom: PSD of the TBFABM for the LES data (left) Kaimal and Mann (middle) and TIMESR (right)

neutral conditions for the LES model. The effect of the 3P and 1P frequencies is the same as the one observed for the models fitted to the FINO-1 measurements. Furthermore, the higher energy content at around 0.003 Hz, which was also noticed in the PSD of the LES data wind fields, is captured by the TIMESR model, but not by the synthetic models.

From Figures 10 and 11, it is seen that the TIMESR model based on three data points from LES data accurately captures the response related to surge and pitch; however, the response related to yaw is not well captured. This is because the points chosen as input to fit the TIMESR model are only vertically, and not horizontally, distributed. Therefore, due to the dependence of yaw on lateral coherence, the responses related to this degree of freedom differ from the LES data.

Due to the significant response at 0.003 Hz, it is of interest to investigate the simulation settings which might impact the wind field at this frequency. To examine the role of the surface heat flux rate on the energy content at 0.003 Hz, we study the below-rated wind speed scenario, under unstable conditions, with heat flux varying from 0.05 to 0.025 km/s and 0.0125 km/s. The shear exponent is the same for the three cases. However, turbulence intensity decreases from 8.9%, for the case with the strongest heat flux, to 5.0%, for the case with the smallest heat flux. The wind field at hub height for the three cases is shown in Figure 12, where the size of the characteristic eddies is qualitatively evident and can be approximated as roughly 2,500 m, related to the 0.003 Hz frequency for the 7.5 m/s scenario.

Figure 13 shows the effect of decreasing the surface heat flux on the platform yaw and the TBFABM. The effect of lower turbulence intensity is seen in both yaw and the structural response. The higher energy content at 0.003 Hz shows up in the three cases, although its intensity decreases with the heat flux rate. Therefore the effect of the heat flux on the turbulence intensity, and thus on the response, should not be neglected. From Figure 13 it is seen that the TBFABM, highly correlated to surge and pitch in general, is properly reproduced by the TIMESR model. The response in yaw is not well captured, due to the dependence of yaw on lateral coherence, which is not reproduced in the TIMESR models, since the input points are only vertically distributed.

Figure 14 presents the standard deviation and PSD of the tension at the fairlead 1. The trend is very similar to the one presented for the models fitted to the FINO-1 measurements. The tension under unstable conditions is larger, due to the higher turbulence intensity and coherence. For the 7.5 m/s wind speed case, it is seen that the Kaimal and Mann models underestimate the response compared to the model based on LES data. For the 12 m/s case, the response is overestimated by the Kaimal model for the three stability conditions. The Mann model underestimates the response under unstable conditions but shows a similar response under neutral and stable conditions. For the 16 m/s wind speed case, the difference between the conditions and models is negligible. The PSD of the responses show that the contribution of the wave is higher with respect to the wind contribution, as the wind speed increases. For the 12 m/s case, the surge natural frequency (0.011 Hz, i.e., at approximately four times 0.003 Hz) is excited, and therefore, a higher response is observed. The higher energy content at 0.003 Hz, related to the size of convective cellular structures, is captured by the TIMESR model.

Figure 15 shows the short-term DEL for the TBFABM, the TTYBM, the BROoPM and the fairlead 1 tension, for the three stability conditions and the three mean wind speed scenarios for the models based on LES data. The TBFABM DEL and the BROoPM DEL show the same trends as the FINO-1 measurements, which are also highly correlated to the surge and pitch global motions. The loading is largest under unstable conditions, regardless of the wind speed scenario and model. The LES model shows a higher loading than the Mann model, but lower than the Kaimal one. The TTYBM DEL presents again the same trend as the one found for the models fitted to the FINO-1 data: Under unstable conditions, the DEL is highest. The DEL of the LES model is in general higher than the TIMESR and Kaimal models, but lower than the Mann model. This
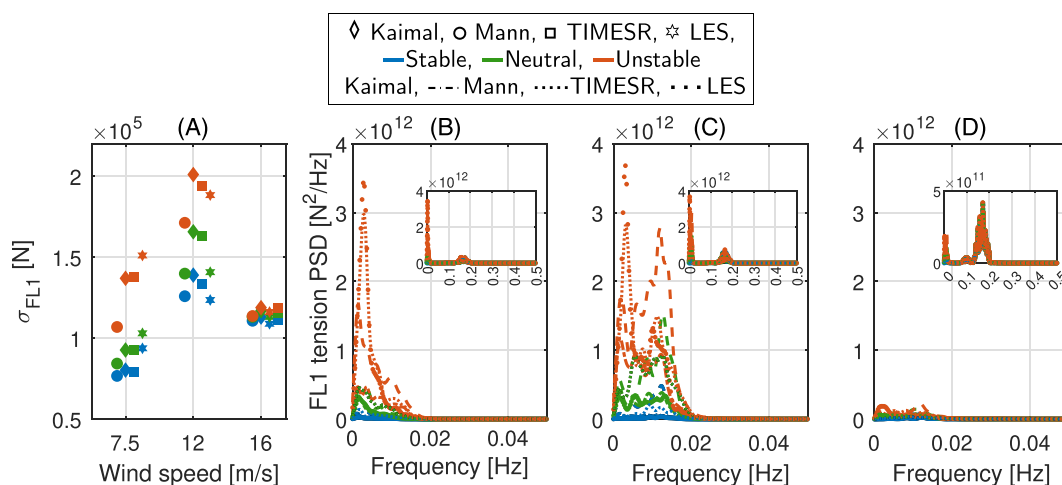

FIGURE 14 (A) Average of the standard deviation of the tension, for the six seeds, at fairlead 1. (B–D) Average of the six seeds of the PSD of the tension at fairlead 1 for 7.5, 12 and 16 m/s, respectively. These results correspond to the models fitted to the LES data
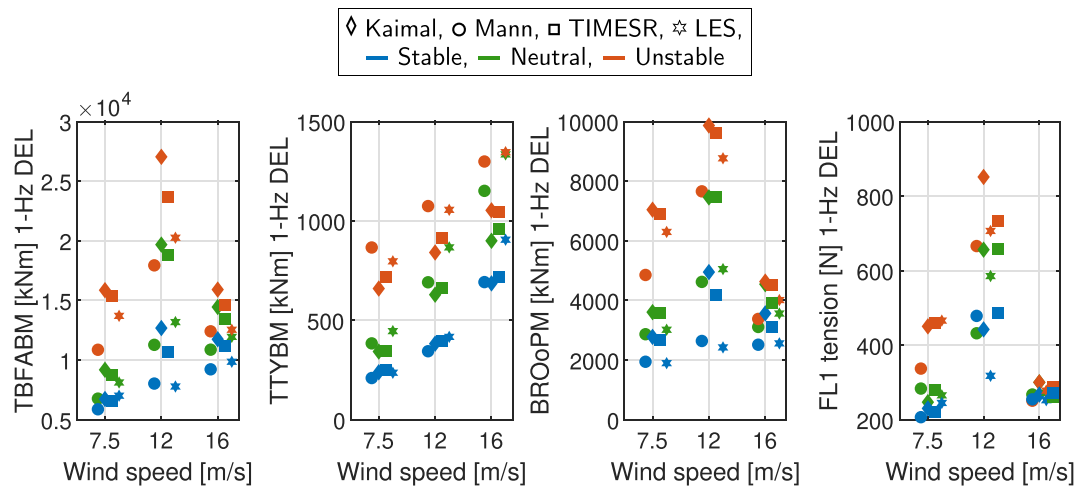
FIGURE 15 Short-term DEL for the TBFABM, TTYBM, BROoPM and FL1 tension, for the models fitted to LES

difference is related to a lower lateral coherence for the LES data and the Mann model and is consistent with the responses in yaw of these two models. The FL1 tension DEL shows very similar trends as for the models fitted to the FINO-1 measurements, and therefore in agreement with previous findings in the literature. The DEL for the LES model itself is very similar to the Kaimal and TIMESR models for every condition for the below- and over-rated scenarios. For the rated wind speed scenario, the DEL for the LES model is lower, which is based on the lower lateral coherence for this case, and is consistent with the lower responses in surge and pitch. Nybø et al[17] also found that the LES model yielded a lower loading than the other models, for the rated case, under stable and neutral conditions, but the opposite for the unstable case, i.e., higher DEL of the mooring line computed by the LES model, compared to the other models. Doubrawa et al[9] found the opposite to what we observe in this work: The DEL of the FL1 tension was higher for the Mann model than for the LES, whereas the Kaimal model showed a lower response than the LES model, for neutral conditions. However, the loading on the fairlead is highly dependent on the design of the mooring lines and the concept itself.

5 | CONCLUSIONS

The IEC guidelines recommend two wind turbulence models for the design and analysis of FWTs; however, these turbulence models are based on neutral stratification and do not account for the varying thermal stratification of the marine atmospheric boundary layer. In this work, we use two approaches to obtaining thermally stratified wind fields. First, we process 2-year of point measurements from the FINO-1 offshore met-mast and second, we use LES to represent high-fidelity wind data. We account for atmospheric stability in the Kaimal and Mann models by fitting their input parameters to both the point measurements and the LES data. Additionally, we use the TIMESR method from the TurbSim wind field generator. This yields four methods to generating turbulent wind: Kaimal, Mann, TIMESR and LES. The wind fields are input to OpenFAST 2.5.0, an aero-hydro-servo-elastic tool that is used to study the low-frequency structural response of the INO WINDMOOR 12MW FWT.

Separate comparisons of the motions and structural response using synthetic models fitted to the measurements and to the high-fidelity data, separately, yield similar conclusions. The Mann model presents a lower lateral coherence for the three mean wind speed scenarios and for the three stability conditions, and consequently, the responses related to yaw are seen to be higher, up to 30% for some cases. For the models fitted to the LES data, comparison against the LES data themselves suggests that the response in yaw is better predicted by the Mann model than by the Kaimal model. However, for the responses related to surge and pitch, the Mann model underpredicts responses compared not only to the high-fidelity data but also to the TIMESR model fitted to the point measurements, yielding a maximum difference of 27% for the surge standard deviation under unstable conditions. The TIMESR model predicts motions and responses quite close to the high-fidelity data, although for the responses where lateral coherence plays a significant role, as is the case for yaw, the responses are underestimated, with up to a 22% difference. The Kaimal model does not show the same underprediction of surge and pitch as seen in the Mann model.

The work presented in this study shows that both atmospheric stability and the wind turbulence model play an important role at the lower-frequency range, where semisubmersible structures have their natural periods. Since high-fidelity data or measurements are not readily available when completing the structural analyses of such structures, we recommend that the parameters of the Kaimal and Mann synthetic models should be rigorously fitted to the most predominant stability conditions where a FWT will operate.

PEER REVIEW

The peer review history for this article is available at https://publons.com/publon/10.1002/we.2775.

ORCID

Irene Rivera-Arreba https://orcid.org/0000-0003-2258-7028
Erin E. Bachynski-Polić https://orcid.org/0000-0002-1471-8254

REFERENCES

1. Sathe A, Mann J, Barlas T, Bierbooms W, van Bussel G. Influence of atmospheric stability on wind turbine loads. *Wind Energy*. 2012;16(7):1013-1032.
2. Liu L, Stevens RJAM. Effects of atmospheric stability on the performance of a wind turbine located behind a three-dimensional hill. *Renew Energy*. 2021;175:926-935.
3. Nybø A, Nielsen F, Godvik M. Quasi-static response of a bottom-fixed wind turbine subject to various incident wind fields. *Wind Energy*. 2021;24(12): 1482-1500.
4. IEC. IEC61400-1: Wind energy generation systems—part 1: design requirements, Geneva, Switzerland, International Electrotechnical Commission; 2019.
5. Kaimal JC, Wyngaard JC, Izumi Y, Coté OR. Spectral characteristics of surface-layer turbulence. *Quart J R Meteorol Soc*. 1972;98(417):563-589.
6. Mann J. The spatial structure of neutral atmospheric surface-layer turbulence. *J Fluid Mech*. 1994;273:141-168.
7. Mann J. Wind field simulation. *Probab Eng Mech*. 1998;13(4):269-282.
8. Haugen DA, Kaimal JC, Bradley EF. An experimental study of Reynolds stress and heat flux in the atmospheric surface layer. *Quart J R Meteorol Soc*. 1971;97(412):168-180.
9. Doubrawa P, Churchfield MJ, Godvik M, Sirnivas S. Load response of a floating wind turbine to turbulent atmospheric flow. *Appl Energy*. 2019;242: 1588-1599.
10. Eliassen L, Obhrai C. Coherence of turbulent wind under neutral wind conditions at FINO1. *Energy Procedia*. 2016;94:388-398.
11. Eliassen L, Bachynski EE. The effect of turbulence model on the response of a large floating wind turbine. In: American Society of Mechanical Engineers. ASME; 2017.
12. Bachynski EE, Eliassen L. The effects of coherent structures on the global response of floating offshore wind turbines. *Wind Energy*. 2019;22:219-238.
13. Wise AS, Bachynski EE. Wake meandering effects on floating wind turbines. *Wind Energy*. 2019;23(5):1266-1285.
14. Putri RM, Cheynet E, Obhrai C, Jakobsen JB. Turbulence in a coastal environment: the case of vindeby. *Wind Energy Sci Discuss*. 2021;2021:1-32.
15. Nybø A, Nielsen FG, Reuder J, Churchfield MJ, Godvik M. Evaluation of different wind fields for the investigation of the dynamic response of offshore wind turbines. *Wind Energy*. 2020;23(9):1810-1830.
16. de Marí M, Mann J. Validation of the Mann spectral tensor for offshore wind conditions at different atmospheric stabilities; 2014. TORQUE, Journal of physics: Conference series.
17. Nybø A, Nielsen F, Godvik M. Sensitivity of the dynamic response of a multimegawatt floating wind turbine to the choice of turbulence model. *Wind Energy*. 2022;25(6):1013-1029.
18. Myrtvedt M, Nybø A, Nielsen F. The dynamic response of offshore wind turbines and their sensitivity to wind field models. *J Phys: Confer Ser*. 2020; 1669(1):012013. https://doi.org/10.1088/1742-6596/1669/1/012013
19. Souza C, Engebretsen E, Bachynski–Polić E, Eliassen L, Berthelsen P, Haslum H. Definition of the ino windmoor 12 mw base case floating wind turbine. *Technical Report*, Trondheim, Norway, SINTEF Ocean; 2021.
20. Jonkman BJ. *Openfast documentation release v2.1.0*. Boulder, Colorado: Office of Scientific and Technical Information (OSTI); 2019. NREL.
21. Jonkman BJ, Buhl M. *TurbSim user's guide*. Boulder, Colorado: Office of Scientific and Technical Information (OSTI); 2005. NREL.
22. Skamarock W, Klemp J, Dudhia J, Gill D, Liu Z, Berner J, Wang W, Powers J, Duda M, Barker D, Huang X-Y. A description of the advanced research wrf model version 4, Boulder, CO, United States, UCAR/NCAR; 2019.
23. Kvittem M, Moan T. Time domain analysis procedures for fatigue assessment of a semi-submersible wind turbine. *Marine Struct*. 2015;40:38-59.
24. Bundesamt für Seeschifffahrt und Hydrographie. FINO - Databankinformationen; 2020.
25. Li L, Gao Z, Moan T. Joint environmental data at five european offshore sites for design of combined wind and wave energy devices. In: Volume 8: Ocean renewable energy. ASME American Society of Mechanical Engineers; 2013.
26. Cheynet E, Jakobsen JB, Snæbjörnsson J, Ágústsson H, Harstveit K. Complementary use of wind lidars and land-based met-masts for wind measurements in a wide fjord. *J Phys: Confer Ser*. 2018;1104:12-28.
27. Pasquill F. The estimation of the dispersion of windborne material. *Meteorol Mag*. 1961;90:33.
28. Krogsæter O, Reuder J. Validation of boundary layer parameterization schemes in the Weather Research and Forecasting (WRF) model under the aspect of offshore wind energy applications—part II: boundary layer height and atmospheric stability. *Wind Energy*. 2014;18(7):1291-1302.
29. Golder D. Relations among stability parameters in the surface layer. *Bound-Layer Meteorol*. 1972;3(1):47-58.
30. Haupt S, Kosović B, Shaw W, et al. On bridging a modeling scale gap: mesoscale to microscale coupling for wind energy. *Bull Am Meteorol Soc*. 2019; 100(12):2533-2550. https://journals.ametsoc.org/view/journals/bams/100/12/bams-d-18-0033.1.xml

31. Monin A, Obukhov A. Basic laws of turbulent mixing in the surface layer of the atmosphere. *Contrib Geophys Inst Acad Sci USSR*. 1954;151(163):e187.

32. Deardorff J. Stratocumulus-capped mixed layers derived from a three-dimensional model. *Bound-Layer Meteorol*. 1980;18(4):495-527.

33. Archer C, Colle B, Veron D, Veron F, Sienkiewicz M. On the predominance of unstable atmospheric conditions in the marine boundary layer offshore of the u.s. northeastern coast. *J Geophys Res: Atmos*. 2016;121(15):8869-8885.

34. Peña A, Kosović B, Mirocha JD. Evaluation of idealized large-eddy simulations performed with the weather research and forecasting model using turbulence measurements from a 250 m meteorological mast. *Wind Energy Sci*. 2021;6(3):645-661.

35. Irwin JS. A theoretical variation of the wind profile power-law exponent as a function of surface roughness and stability. *Atmos Environ (1967)*. 1979; 13(1):191-194.

36. Emeis S. Current issues in wind energy meteorology. *Meteorol Appl*. 2014;21(4):803-819.

37. Kretschmer M, Jonkman J, Pettas V, Cheng P. FAST.Farm load validation for single wake situations at Alpha Ventus. *Wind Energy Sci*. 2021;6(5): 1247-1262.

38. Cheynet E. Numerical implementation of the uniform shear model. https://github.com/ECheynet/MannModel1994/releases/tag/v1.7, Accessed: 2021-09-30; 2021.

39. Welch P. The use of fast fourier transform for the estimation of power spectra: a method based on time averaging over short, modified periodograms. *IEEE Trans Audio Electroacoust*. 1967;15(2):70-73.

40. Cheynet E, Jakobsen JB, Reuder J. Velocity spectra and coherence estimates in the marine atmospheric boundary layer. *Bound-Layer Meteorol*. 2018; 169(3):429-460.

41. Chougule A. Influence of atmospheric stability on the spatial structure of turbulence. *Ph.D. Thesis*: Technical University of Denmark; 2013.

42. Veers P. Modeling stochastic wind loads on vertical axis wind turbines. In: 25th structures, structural dynamics and materials conference. American Institute of Aeronautics and Astronautics AIAA; 1984.

43. DTU Wind Energy. Pre-processing tools—hawc2. Technical University of Denmark, Copenhagen, Denmark; 2014.

44. Robertson A, Sethuraman L, Jonkman J, Quick J. Assessment of wind parameter sensitivity on ultimate and fatigue wind turbine loads: Preprint, Boulder, CO, United States, NREL; 2018.

45. Simon J, Zhou B, Mirocha J, Chow F. Explicit filtering and reconstruction to reduce grid dependence in convective boundary layer simulations using wrf-les. *Monthly Weather Rev*. 2019;147(5):1805-1821. https://journals.ametsoc.org/view/journals/mwre/147/5/mwr-d-18-0205.1.xml

46. Göçmen T, Larsén X, Imberger M. The effects of open cellular convection on wind farm operation and wakes. *J Phys: Confer Ser*. 2020;1618(6): 062014. https://doi.org/10.1088/1742-6596/1618/6/062014

47. Hayman GJ, Buhl M. *MLife User's Guide Version 1.00*. Boulder, CO, United States; NREL; 2013.

48. Hayman GJ. MLife Theory Manual MLife Theory Manual Version 1.00. NREL, Boulder, CO, United States; 2013.

49. SINTEF Ocean. Simo theory manual. SINTEF Ocean, Trondheim, Norway; 2019.